A two-dimensional conjugated aromatic polymer via C–C coupling reaction

Wei Liu[1,2,3†], Xin Luo[2†], Yang Bao[1,2,3†], Yan Peng Liu[1], Guo-Hong Ning[1], Ibrahim Abdelwahab[1,3], Linjun Li[2], Chang Tai Nai[1], Zhi Gang Hu[4], Dan Zhao[4], Bin Liu[4], Su Ying Quek[2,5★] and Kian Ping Loh[1,2★]

The fabrication of crystalline 2D conjugated polymers with well-defined repeating units and in-built porosity presents a significant challenge to synthetic chemists. Yet they present an appealing target because of their desirable physical and electronic properties. Here we report the preparation of a 2D conjugated aromatic polymer synthesized via C–C coupling reactions between tetrabromopolyaromatic monomers. Pre-arranged monomers in the bulk crystal undergo C–C coupling driven by endogenous solid-state polymerization to produce a crystalline polymer, which can be mechanically exfoliated into micrometre-sized lamellar sheets with a thickness of 1 nm. Isothermal gas-sorption measurements of the bulk material reveal a dominant pore size of ~0.6 nm, which indicates uniform open channels from the eclipsed stacking of the sheets. When employed as an organic anode in an ambient-temperature sodium cell, the material allows a fast charge/discharge of sodium ions, with impressive reversible capacity, rate capability and stability metrics.

The discovery of graphene, the archetypal two-dimensional (2D) sheet of sp^2-hybridized carbon, has stimulated interest in the rational organic synthesis of π-conjugated 2D polymers, which are expected to offer greater flexibility in terms of composition, topology and other physical properties compared with graphene[1–3]. Quantum confinement in single or few-layer thick 2D organic sheets is expected to lead to emergent phenomena, in addition to applications in flexible optoelectronic devices. Although there are a multitude of methods to polymerize molecules to produce linear, crosslinked or branched polymers with a diverse range of functional groups and properties, the synthesis of crystalline 2D polymers that comprise repeating units that can create topologically planar macromolecules (rather than linear) has met with much less success[4,5]. Constructing 2D conjugated polymers with strong and stable linkages, such as C–C bonds, has been a long-sought aim of chemists[3,5,6].

Müllen and co-workers demonstrated the structurally precise synthesis of graphene-like polycyclic aromatic hydrocarbons[7–9]. These graphene fragments of various sizes, shapes and edges exhibit promising optoelectronic properties because of the quantum confinement and their specific edge structure[7–9]. Surface-templated strategies have been applied successfully to the preparation of 2D-conjugated molecular nanostructures[10–12]. A wide variety of molecular networks has been synthesized through aryl–aryl coupling on substrate surfaces under ultrahigh vacuum (UHV) conditions with crystalline domains in the range of a few hundred square nanometres[10,11]. Molecular framework approaches offer advantages over surface strategies because they allow bulk synthesis on a larger scale[5,13]. Among them, 2D covalent organic frameworks (COFs) constructed by linkages, such as imine[14,15] and phenazine[16], under reversible bond-forming conditions possess an in-plane conjugated periodic porous structure. Covalent triazine frameworks are also examples of molecular platforms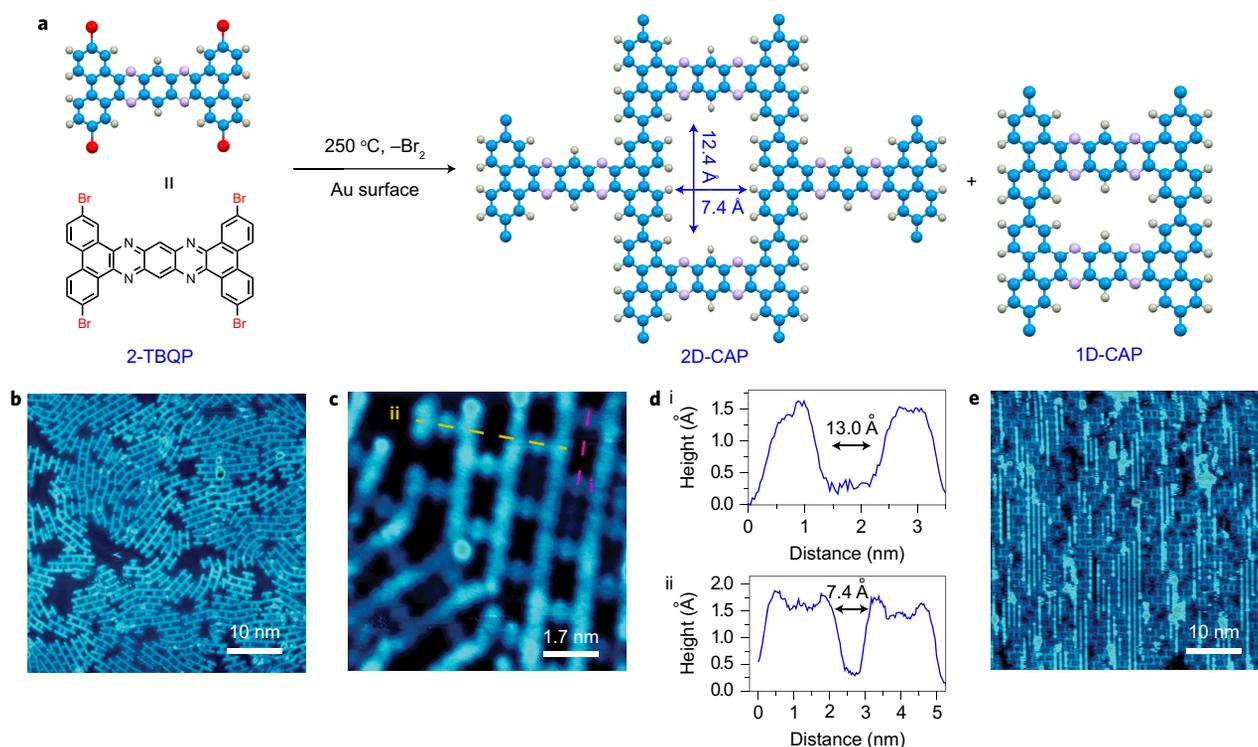 that possess intrasheet conjugation[17,18]. However, the construction of COFs with strong bonds, such as C–C bonds, has not yet been achieved[5].

Recently, crystal engineering was shown to be an elegant approach to non-conjugated 2D polymers through the reversible self-addition polymerization between 2D-confined monomers in single crystals[19–22]. Separating the crystallization process from the step at which bond formation occurs, as is the case for the single-crystal approach, usually enables a higher-quality crystallization. Consequently, the prepared lamellar polymers are in the form of single crystals that can be exfoliated into monolayer polymeric crystal[20,21]. Here we designed a precursor 2-TBQP (2,7,13,18-tetrabromodibenzo[a,c]dibenzo[5,6:7,8]quinoxalino-[2,3-i]phenazine), from which a crystalline 2D-conjugated aromatic polymer (2D-CAP) can be constructed by C–C coupling of the monomers in the crystalline state. The synthesized 2D-CAP shows a distinct lamellar structure, from which ultrathin 2D sheets can be exfoliated. Furthermore, 2D-CAP has a highly uniform pore size of ~0.6 nm, which is a result of the aligned 1D open channels created by the stacking of 2D-CAP sheets. We found that the well-defined channels in 2D-CAP can be exploited for energy storage in sodium ion batteries (NIBs). When 2D-CAP is employed as an organic anode in an ambient-temperature sodium cell, it gives a reversible capacity of 114 mAh g^{-1} at a high current density of 5.0 A g^{-1} and retains 70% of its capacity after 7,700 cycles.

Results and discussion

Synthesis and characterization. The phenazine ring-fused molecule 2-TBQP (Fig. 1a) was prepared through a condensation reaction between 2,7-dibromophenanthrene-9,10-dione (2,7-DBPD) and benzene-1,2,4,5-tetraamine in quantitative yield (Supplementary Fig. 1). To examine how crosslinking between the 2-TBQP monomers can produce a 2D network (Fig. 1a), we first performed metal-surface-mediated polymerization between individual 2-TBQP molecules adsorbed on Au(111). The resulting monolayer film was

[1]Department of Chemistry, National University of Singapore, 3 Science Drive 3, Singapore 117543, Singapore. [2]Centre for Advanced 2D Materials (CA2DM), National University of Singapore, 6 Science Drive 2, Singapore 117546, Singapore. [3]NUS Graduate School for Integrative Sciences and Engineering, National University of Singapore, Centre for Life Sciences, #05-01, 28 Medical Drive, Singapore 117456, Singapore. [4]Department of Chemical and Biomolecular Engineering, National University of Singapore, 4 Engineering Drive, Singapore 117585, Singapore. [5]Department of Physics, National University of Singapore, 2 Science Drive 3, Singapore 117551, Singapore †These authors contributed equally to this work. *e-mail: phyqsy@nus.edu.sg; chmlohkp@nus.edu.sg
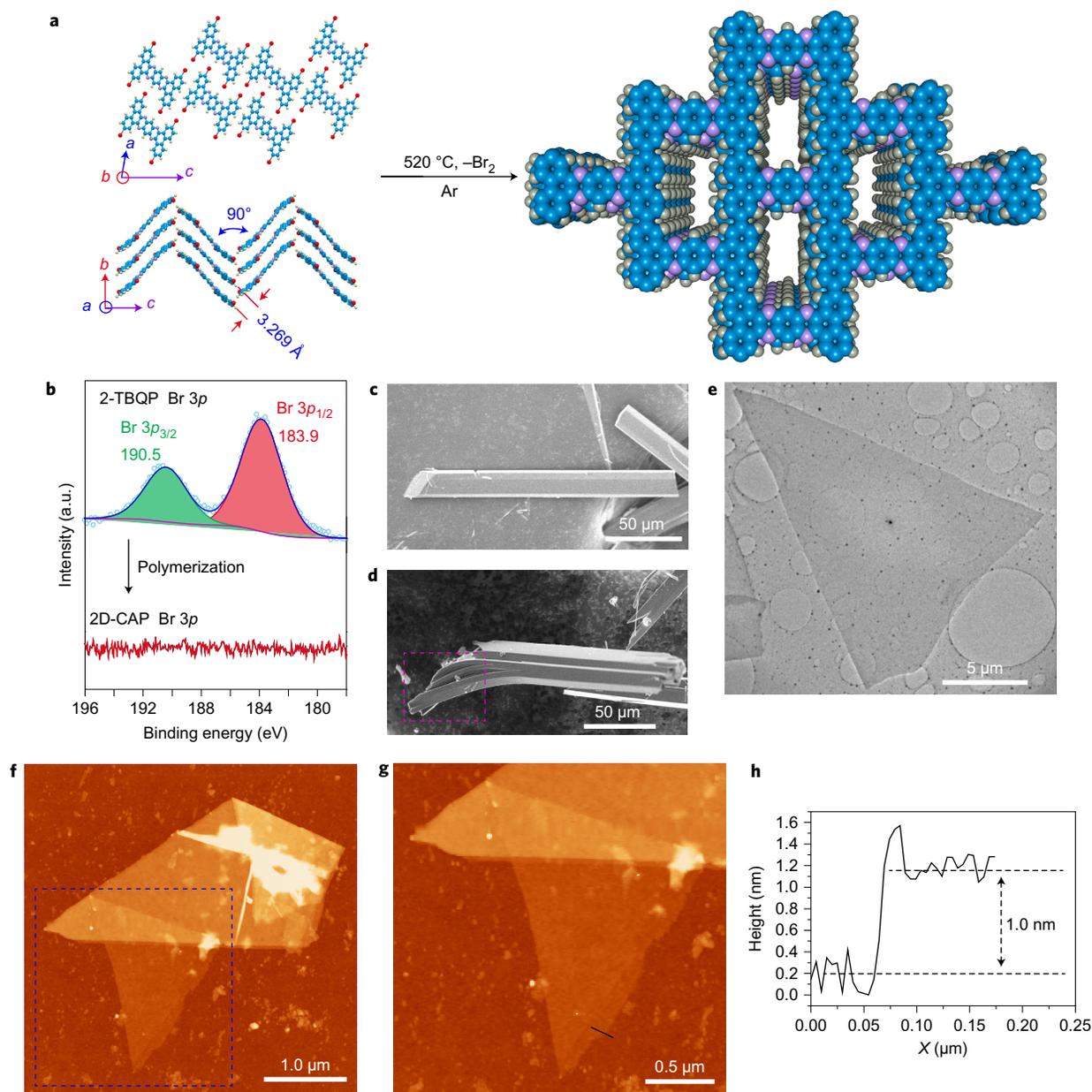
Figure 1 | STM characterization of a single-layer CAP on a Au surface prepared by surface-mediated polymerization. a, Synthesis of CAP by the metal-surface-mediated polymerization of 2-TBQP. **b**, Single-layer CAP grown on a Au(111) surface. **c**, Two misoriented 2D-CAP domains on a Au(111) surface. **d**, Corresponding height profiles for cross-sections i (pink) and ii (yellow) in **c**. **e**, Single-layer CAP grown on a Au(110) surface.

characterized by scanning tunnelling microscopy (STM). On Au(111), at first the individual 2-TBQP molecules adsorb with no apparent order. At an elevated temperature of 250 °C, the precursor molecules undergo surface-assisted debromination and aryl–aryl coupling[10] to form a rectangular-grid network (Fig. 1b,c). STM height profiles of the 2D-CAP grid show that its pore sizes are ~13.0 Å along the long axis (Fig. 1d,i) and ~7.4 Å along the short axis (Fig. 1d,ii), which match well with the theoretical dimensions of the pores in the single-layered 2D-CAP (Fig. 1a). Some misoriented 2D-CAP domains are observed (Fig. 1b,c) because of the free rotation of 2-TBQP monomers on the Au(111) surface during the polymerization process. To reduce the rotational misorientation, anisotropic Au(110) was used as the growth substrate. Au(110) is characterized by the (1×2) missing row reconstruction of the topmost Au atoms[23], which allows molecules to diffuse favourably along the missing-row direction. After thermal activation of the adsorbed 2-TBQP molecules at 250 °C, a better orientation of the grid network was, indeed, obtained (Fig. 1e). A closer examination of the STM images (Fig. 1b,e and Supplementary Fig. 12) shows that, besides 2D-CAP, there are also a few 1D-CAPs, an unfavourable product of the polymerization. These observations are in agreement with first-principles density functional theory (DFT) calculations. The calculated formation energy per monomer of the 2D-CAP is energetically more favourable than that of the 1D-CAP by 0.04 eV (Supplementary Fig. 13 gives the details). The irreversible C–C bond formation prevents self-correction, which means that 1D-CAP, once formed, introduces defects to the 2D network and reduces its crystallinity.

These studies therefore show that C–C cross-couplings among the monomers can generate a periodic 2D-CAP network if the kinetic factors can be optimized to suppress the formation of 1D-CAPs. Generally, it is difficult to prepare crystalline 2D- or 3D-conjugated polymers through dehalogenation-type C–C coupling. For example, conjugated porous polymers synthesized through Yamamoto coupling are usually amorphous as long-range periodicity cannot be attained owing to the irreversible reactions between randomly aligned monomers[24,25]. A better strategy may be pre-ordering the monomers to facilitate well-defined C–C coupling in a solid-state endogenous crystal-to-polycrystal conversion.

To test our hypothesis, 2-TBQP molecules were sublimated and recrystallized in a tube furnace. Needle-like single crystals of 2-TBQP millimetres to centimetres in length were obtained (Supplementary Fig. 3). The structure was solved by single-crystal X-ray diffraction (XRD) analysis, which revealed a zigzag and tightly packed lamellar structure through a displaced face-to-face π–π interaction at a distance of 3.269 Å (Fig. 2a). Phenazine ring-fused organic compounds are well known for their thermal stability[26,27], and thermal gravimetric analysis revealed that 2-TBQP has only one obvious weight-loss stage that starts at 520 °C, which is the onset temperature for the debromination (a detailed analysis is given in Supplementary Fig. 2). After holding the temperature at 520 °C for six hours, the red single crystals turned into a shiny grey needle-shaped polymer. To monitor the debromination process, we carried out X-ray photoelectron spectroscopy (XPS) (Fig. 2b), elemental analysis (Supplementary Table 1) and Fourier transform infrared spectroscopy (Supplementary Fig. 7) of 2-TBQP before and after the endogenous solid-state polymerization, which revealed that the bromine had largely vanished. 2-TBQP displays an absorbance peak in the ultraviolet and visible regions from 250 to 650 nm, whereas the polymer shows a much broader absorbance range from the ultraviolet to near-infrared regions (1,350 nm), which indicates an extended delocalization of the π-conjugated skeleton after polymerization (Supplementary Fig. 8). Scanning electron microscopy (SEM) studies revealed that the bulk precursor 2-TBQP crystal (Fig. 2c) changed into polymers with clear lamellar features (Fig. 2d). The embedded polymeric sheets are parallel to the c axis of the original precursor 2-TBQP crystal. These crystals can be readily exfoliated by Scotch tape into micrometre-sized,
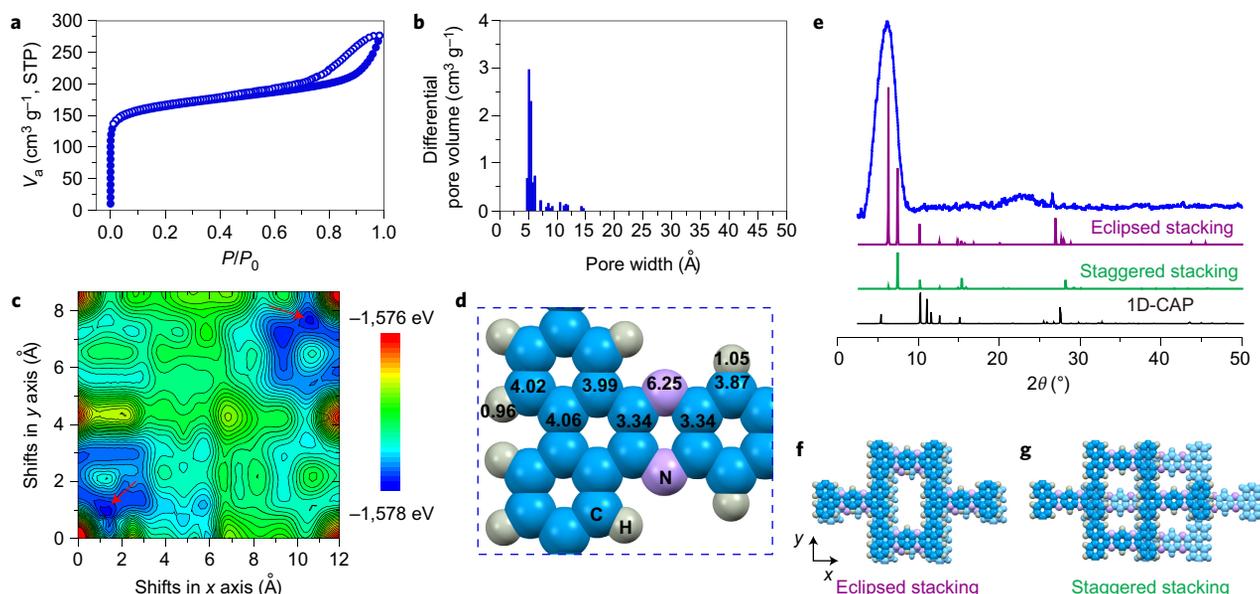
Figure 2 | Synthesis and characterization of 2D-CAP via endogenous solid-state polymerization. a, Polymerization conditions and crystallographic packing of 2-TBQP shown as a ball-and-stick model (top, top view; bottom, side view). **b**, XPS Br 3p spectra of 2-TBQP and 2D-CAP. **c**, SEM image of 2-TBQP crystals. **d**, SEM image of the as-prepared 2D-CAP crystals. The slightly twisted part in the pink dashed rectangle area reveals a clear lamellar structure. **e**, TEM image of an exfoliated 2D-CAP sheet. **f**, AFM topography of exfoliated 2D-CAP sheets on a silicon wafer. **g**, AFM topography of the triangular sheet (marked with the purple dashed square) in **f**. **h**, Corresponding AFM height profile for the cross-section in **g** (black line) shows that step edge has a height of ~1 nm. a.u., arbitrary units.

nanometre-thick sheets. Figure 2e shows a triangular sheet with sides ~15 µm in length and neat edges under a transmission electron microscope (TEM). The exfoliated sheets were transferred onto a silicon wafer and the lamellar features were confirmed by atomic force microscopy (AFM) investigations. Figure 2f shows a triangular sheet that partially covers the top of another sheet with neat edges. An AFM height profile revealed that the thickness was ~1 nm (Fig. 2h), similar to that of single-layer graphene[1].

We further probed the porosity of 2D-CAP by Ar adsorption/ desorption isotherm measurements. 2D-CAP shows a type 1 isotherm, which is typical for microporous absorbents with a signifi- cant uptake in the low-pressure region ($P/P_0 < 0.1$) (Fig. 3a). The small hysteresis branches in the high-pressure region ($P/P_0 > 0.8$)

can be ascribed to the interparticle voids of the powder product. The Brunauer–Emmett–Teller (BET) surface area was evaluated as $SA_{BET} = 539$ m^2 g^{-1}, which is in the range reported for 2D COFs[13], and the pore volume was 0.35 cm^3 g^{-1}. The product gener- ated by heating the non-brominated analogue dibenzo[a,c]dibenzo [5,6:7,8]quinoxalino[2,3-i]phenazine (DDQP, as shown in Supplementary Fig. 1) showed no obvious porous structure (Supplementary Fig. 11). The very narrow peak in the pore- volume plot indicates that the pore width is quite homogeneous and was estimated to be ~0.6 nm (Fig. 3b). To determine the pore size in 2D-CAP, DFT calculations were carried out to map the energy surface as a function of slip distances between adjacent sheets of bulk 2D-CAP, as shown in Fig. 3c. The lowest-energy
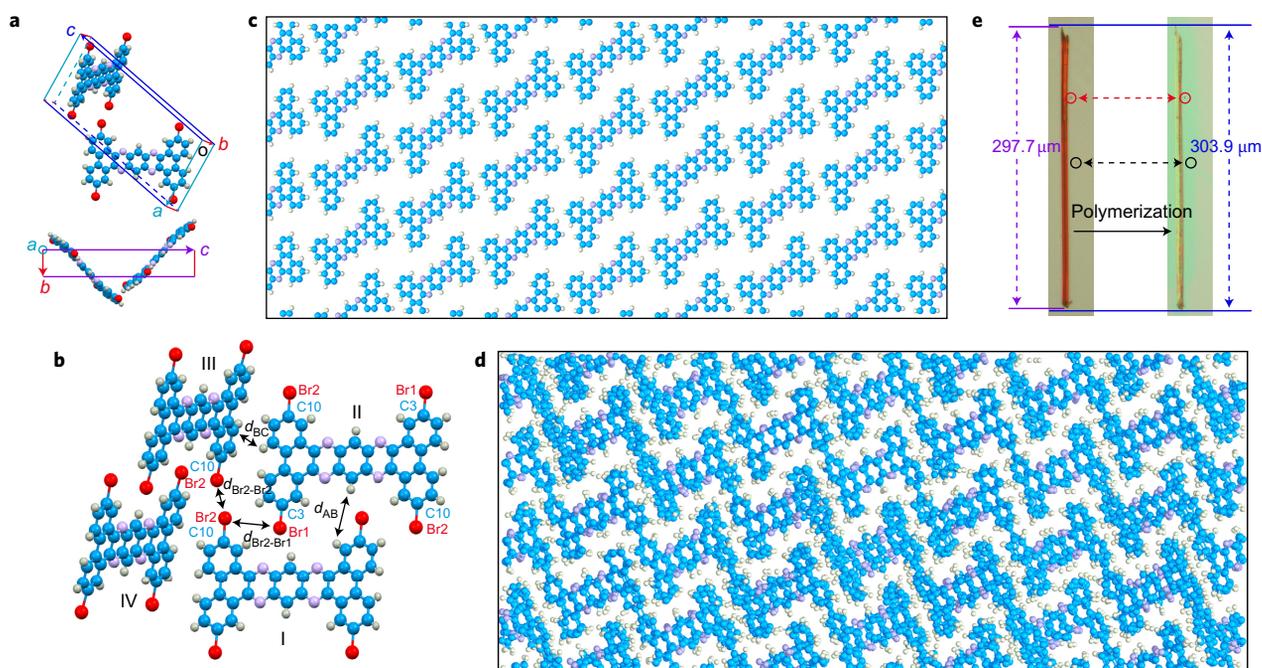
Figure 3 | Isotherm profiles of Ar-gas sorption and crystalline structure analysis of 2D-CAP. a, Ar adsorption (filled) and desorption (open) isotherm profiles of 2D-CAP. **b**, Pore-size distribution of 2D-CAP calculated by non-local DFT modelling based on Ar-adsorption data. **c**, Energy surface of bulk 2D-CAP with different slip distances between two adjacent layers (the bottom-left and top-right corners correspond to AA stacking, the bottom-right and top-left corners correspond to AB (staggered) stacking). The two red arrows indicate the two equivalent lowest-energy areas. **d**, Bader charge analysis of 2D-CAP. The number on each labelled atom represents the number of valence electrons on the atom. **e**, XRD profile obtained on 2D-CAP (blue) and simulated XRD patterns using an eclipsed stacking mode (purple), staggered stacking mode (green) and 1D-CAP (black; the optimized 1D-CAP structure is included in Supplementary Fig. 15). **f**, Top view of the optimized 2D-CAP in the eclipsed stacking mode. **g**, Top-view of the optimized 2D-CAP in the staggered stacking mode. STP, standard temperature and pressure.

structure is close to AA stacking, but with a 1.4 Å slip along the *x*-axis direction and a 1.0 Å slip along the *y*-axis direction, as shown by the two lowest-energy areas in Fig. 3c, which are equivalent because of the symmetry of the 2D-CAP layer. The eclipsed stacking arises from the interplay between the repulsive Coulomb interaction that originated from the negatively charged N atoms on an adjacent sheet and the attractive Coulomb interactions between the negatively charged N atoms on one sheet and the positively charged C atoms on the adjacent sheet. These positively charged C atoms are the atoms that are bonded directly to electron-withdrawing N, as shown by the Bader charge analysis in Fig. 3d and Supplementary Fig. 14. The DFT-optimized lattice parameters and atomic coordinates of the bulk 2D-CAP crystal based on the eclipsed stacking reproduce the experimental XRD profile of the 2D-CAP crystalline polymer. As shown in Fig. 3e, there is a good match between experiment (blue curve) and theory (purple curve) for the (110) peak at ~6.2° and the (002) peak at ~26.7°, which is associated with the interlayer distance and its presence is indicative of a good stacking order. The peak at 7.4°, which corresponds to the (200) facet, may also contribute to the broadness of the experimentally observed XRD peak. The DFT-optimized bulk 2D-CAP structure gives a pore width of 6.0 Å, in agreement with the Ar sorption measurements in Fig. 3b. Taken together, the agreement between theory and experiment, and the lamellar structure of the product, strongly suggest that 2D-CAP is the predominant product of the endogenous solid-state polymerization. The deep energy minimum (Fig. 3c) caused by the Coulombic interactions also makes the presence of stacking faults unlikely, which give rise to the formation of ordered 1D open channels[16,28].

Earlier, we discussed that solid-state polymerization starting from the solid-crystal form of 2-TBQP was performed to form 2D-CAP selectively as the desired end product. In Figs 2 and 3, we provide evidence that points to this preferred formation of 2D-CAP after solid-state polymerization. Compared with the reaction on the surface, a solid-state polymerization is expected to be

hindered kinetically by steric considerations according to the arrangement of monomers in the crystal. We now describe the crystal structure of 2-TBQP, in which monomer units are pre-organized to facilitate solid-state polymerization. X-ray crystallographic analysis of 2-TBQP revealed a zigzag and tightly packed structure though a displaced face-to-face π–π interaction (Figs 2a and 4b). In the unit cell of the 2-TBQP crystal, there are two monomers (Fig. 4a). As shown in Fig. 4b, monomers II and III, which are approximately perpendicular to each other, interact via the CH/π interaction with distances that range from 2.823 Å to 3.454 Å. Monomers I and III interact via van der Waals interaction between the Br2 atoms, where $d_{Br2-Br2}$ is 3.716 Å, shorter than the sum of their van der Waals radii (3.9 Å). The close proximity of Br2 atoms strongly favours the expulsion of molecular bromine, and thus the concomitant C10–C10 coupling[29,30]. C10–C10 coupling would lead naturally to 2D-CAP, in which the C3 atoms on I and III would couple to other monomers.

As the reaction occurs in the solid state, in which complete rotation about the as-formed C–C bond is hindered, the identity of the carbon atoms that couple to form the intermonomer C–C bonds is critical to determining the end product formed. Specifically, a C10–C10 coupling would result in the 2D-CAP structure, but a C3–C10 coupling would result in the 1D-CAP structure (Fig. 4b). To determine the probability of forming C10–C10 bonds versus C3–C10 bonds, molecular dynamics simulations using the ReaxFF force field were performed. A constant pressure and temperature ensemble (NPT) was used with periodic boundary conditions. The periodic box for the simulation consists of a 4 × 4 × 4 supercell (6,656 atoms) of bulk 2-TBQP (with bromine atoms removed from the monomers). Bromine atoms were removed as we are concerned with the rearrangement of radicals after the debromination, rather than the debromination process itself. The debromination process may further increase the chance of forming C10–C10 bonds, as discussed above, but this is not considered here. The temperature of the simulation was chosen to be
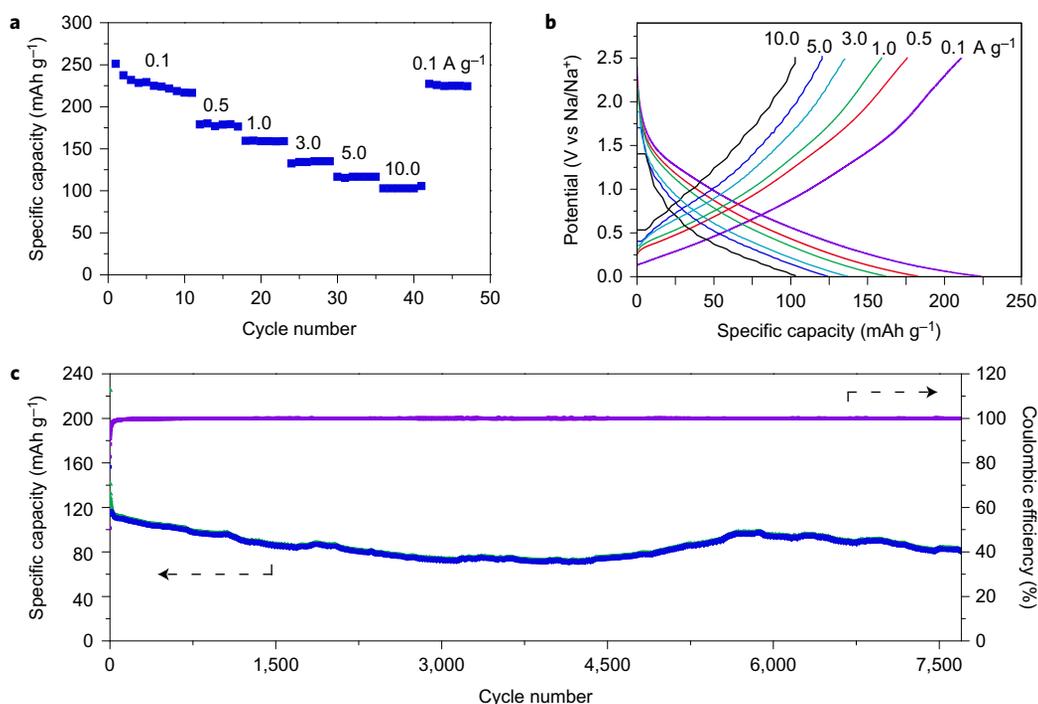
Figure 4 | Reaction-mechanism analysis. a, Unit cell of the 2-TBQP single crystal contains two monomers that are approximately perpendicular to each other; o is the origin of the coordinate system. **b**, Crystallographic parameters between adjacent monomers in 2-TBQP single crystal: $d_{Br2-Br2}$ = 3.716 Å, $d_{Br2-Br1}$ = 4.605 Å, d_{BC} = 2.823 Å, d_{AB} = 4.728 Å. **c,d**, Structural evolution during a molecular dynamics simulation (NPT ensemble) of the bulk 2-TBQP crystal with the bromines removed: top view of the initial precursor structure (**c**) and the formation of C10–C10 connections after 0.1 ns (**d**). No C3–C10 connections are present. **e**, Photographs of crystal deformation recorded at room temperature of the sample before (left) and after (right) the endogenous solid-state polymerization. The sample elongated along the long axis by ~2.1% during the polymerization. The long axis of the crystal is parallel to the crystallographic c axis of the original 2-TBQP. The two crystal fragments in the red and black circle areas serve as markers.

800 K (similar to the temperature of 793 K used in the experiment), the pressure 0 MPa and the time step for the simulation 0.25 fs. Four runs were performed using the C/H, C/C and C/N interaction parameters given by the force field in Newsome *et al.*[31]. In all cases, an analysis after 400,000 time steps (0.1 ns) yields about 125 (124–127) C–C connections, of which all are C10–C10 connections. No C3–C10 connections were present. The exclusive formation of C10–C10 bonds was also observed using other force fields[32,33]. Thus, we have clearly shown that the arrangement of monomers in the 2-TBQP crystal strongly favours C10–C10 coupling over C3–C10 coupling, as required for the preferred formation of 2D-CAP. Details of the molecular dynamics trajectories are shown in Supplementary Fig. 16. After C10–C10 coupling, the dihedral angle between the two connected monomers (I and III in Fig. 4b) is ~90°. DFT calculations further suggest that it is energetically favourable locally for the dihedral angle at the C10–C10 bond to relax from ~90° to 180° (Supplementary Fig. 17). Furthermore, coplanar stacking would be favoured because of the π–π interaction[34]. This is also the case for crystals of other aromatic compounds[35,36]. Planarization is not observed within the timescale of our molecular dynamics simulations but, as shown in Fig. 4e, after solid-state polymerization in the experiment, the needle-shaped single crystal of 2-TBQP (left, 297.6 μm) on the silicon wafer expanded its long (c) axis by approximately 2.1% to 303.9 μm (right), which is consistent with sheet planarization. In the real experiment, C–Br bonds were not broken at the same time, which results in unevenly evolved C–C coupling in the bulk crystal. Consequently, the domain size of the resulting 2D polymer is limited, which leads to the broadness in the XRD profile (Fig. 3e) and the Raman spectrum. Supplementary Fig. 18 shows the experimental Raman spectrum collected for the exfoliated 2D-CAP sheet on a silicon wafer. It matches well with the theoretical Raman signal generated with the ideal 2D-CAP single layer, except

for the broadening feature that resulted from the boundary scattering between crystalline domains of limited size, which is consistent with the nanocrystalline nature of 2D-CAP.

Performance as an organic anode. Conjugated 2D-CAP consists of aligned 1D open channels of ~0.6 nm in diameter, which can potentially provide fast and smooth diffusion pathways for charge storage. Sodium ion batteries (NIBs) are considered as promising candidates for large-scale energy-storage devices in intermittent renewable energy and a smart grid, for which a low-cost, high-power capability and a long-term stability are particular important[37,38]. A fundamental challenge in this area is to surmount the sluggish kinetics and destructive effects associated with electrochemical insertion/extraction of Na ions, owing to their larger radius than that of Li ions, which renders most high-performance lithium ion battery anode materials unsuitable for NIBs[38,39]. Recent studies show that porous polymers with continuous interspaces are promising for smooth and stable reversible-charge storage[40,41]. However, there are scant reports on the use of porous polymers as anodes for sodium storage. To interrogate the sodium-storage ability of 2D-CAP, to make the anode we fabricated coin cells with the composition 75 wt% of synthesized 2D-CAP mixed with 10 wt% of Super P conductive carbon and 15 wt% of sodium alginate. This was combined with metallic Na counter electrodes to fabricate a half-cell to evaluate the electrochemical performance. That only a low weight percentage of conductive carbon was added attests to the conductive nature of 2D-CAP. Figure 5a shows galvanostatic charge capacities of 2D-CAP at various current densities. A 2D-CAP-based electrode was charged to 2.5 V (versus Na/Na+) after a discharge to 0.005 V at a low current density of 0.1 A g⁻¹. The 2D-CAP electrode showed a reversible charge capacity of 250 mAh g⁻¹ at the first cycle and achieved a stable capacity of ~216

Figure 5 | Sodium storage performance of 2D-CAP electrode in the potential range 0.005–2.5 V (versus Na/Na$^+$). a, Charge capacities of the 2D-CAP electrode at 0.1, 0.5, 1.0, 3.0, 5.0 and 10.0 A g^{-1}. **b,** Galvanostatic charge–discharge profiles of 2D-CAP at different current densities. **c,** Cycle performance of 2D-CAP up to 7,700 cycles at 5.0 A g^{-1}.

mAh g^{-1} after ten cycles. Supplementary Fig. 19a shows a typical cyclic voltammogram of 2D-CAP. In the first negative scan, there are two irreversible reduction peaks at 0.7 and 0.4 V, which are generally ascribed to the decomposition of electrolyte and the formation of a solid electrolyte interface (SEI) on the surface of active materials[42,43]. In the third and fifth cycles, no obvious change was observed, which indicates that 2D-CAP is stable in the subsequent cycles. As presented in Supplementary Fig. 19b, the first cycle coulombic efficiency of 2D-CAP at 0.1 A g^{-1} is ~51% and approached almost 100% after the initial few cycles. The irreversible part is mainly contributed by the formation of SEI.

As shown in Fig. 5a, 2D-CAP reached stable capacities of 185, 159, 135 and 118 mAh g^{-1} at 0.5, 1.0, 3.0 and 5.0 A g^{-1}, respectively. A stable capacity of 105 mAh g^{-1} could be obtained at a high current density of 10.0 A g^{-1}. Remarkably, this is about a 50% capacity retention for a two-order increase in the charging/discharging current density from 0.1 to 10.0 A g^{-1} in an ambient sodium cell. Figure 5b shows the discharge–charge profiles of 2D-CAP at different current densities. Most noteworthy is the long-term cycling stability of 2D-CAP at a high-power output. The 2D-CAP sodium cell anode achieved an excellent cycle performance over 7,700 cycles and retained 70% of its initial capacity of ~114 mAh g^{-1} at a high current density of 5.0 A g^{-1} (Fig. 5c). The small rise in capacity at around the 4,500th cycle can be ascribed to the gradual penetration of electrolyte into the nanoporous structure, which facilitates the conduction of sodium ions as well as the activation of the electrode[44,45]. In addition, an organic gel-like film that is reversibly formed on the interface of the active materials may also provide additional charge-storage sites through pseudocapacitive processes[46,47]. A comparison of the sodium storage performance of 2D-CAP with reported sodium cell anodes is presented in Supplementary Table 3. In terms of a high power output and stability, 2D-CAP is superior to all those given in Supplementary Table 3. The superior storage performance of sodium originates from the open channels in the π-conjugated porous structure, which allows a fast and smooth Na$^+$ diffusion.

An electrochemical impedance spectroscopy study provided further evidence for the structural stability of the electrode (Supplementary Fig. 19c). Nyquist plots of the 2D-CAP electrode after charging to 2.5 V at the first, 1,000th and 5,000th cycle show no significant increase of the impedance value between the first and 5,000th cycle, which suggests good electrical contact and charge transport in the 2D-CAP based electrode.

Conclusions

In summary, we have successfully synthesized a crystalline 2D-conjugated aromatic polymer (2D-CAP) by the endogenous solid-state polymerization of a molecular crystal based on C–C coupling. The 2D-CAP crystalline polymer has a layered stacking structure and can be readily exfoliated into ultrathin sheets. 2D-CAP also has a highly ordered porosity (pore size ~0.6 nm) created by the eclipsed stacking of 2D-CAP sheets. Due to its intra-sheet conjugation and ordered open 1D channel, 2D-CAP exhibits unprecedented cycle stability and rate capability when applied as an anode in an ambient-temperature sodium cell. Molecular dynamics simulations showed that for the solid-state polymerization reaction, C–C coupling only occurs at specific C sites that favour the formation of 2D-CAP. The endogenous solid-state polymerization route described here can be applied to other classes of halogenated monomers for which solid-state polymerization based on a C–C coupling reaction may also give rise to a crystalline polymer with a highly regular porosity. The approach presented here opens a new avenue to construct novel 2D polymers with highly regular porosity and chemical stability, which is currently a major challenge in synthetic chemistry.

Methods

Synthesis of 2-TBQP. 2,7-DBPD (0.76 g, 2.1 mmol), and benzene-1,2,4,5-tetraamine tetrahydrochloride (0.28 g, 1.0 mmol) were transferred into a round-bottom flask and suspended in 6 ml of ethanol and 20 ml of acetic acid to make a brown suspension in an Ar atmosphere with stirring, and heated to 100 °C. After the addition of 1.0 ml of triethylamine, the mixture immediately changed to a red colour, and was further refluxed at 130 °C for 6 h. Once cooled to room temperature,

the mixture was diluted with acetic acid and poured into 200 ml of water. The red precipitate was collected and exhaustively washed by soxhlet extraction with water, ethanol, chloroform, THF, N,N-dimethylformamide and ethanol again, and dried at 120 °C overnight to yield 2-TBQP as a copper-coloured powder in quantitative yield. Elemental analysis (%): calculated for ($C_{34}H_{14}Br_4N_4$): C, 51.16, H, 1.77, N, 7.02, Br, 40.05; found: C, 50.72, H, 2.05, N, 7.11, Br 39.93. High-resolution mass spectrometry (negative mode) $m/z = 797.7895$ (Supplementary Fig. 4), calculated for $C_{34}H_{14}Br_4N_4$, 797.7911; no solution NMR data were collected because of 2-TBQP's poor solubility. Its structure was confirmed with single-crystal XRD analysis.

2-TBQP single-crystal growth. Crystals were grown in a three-zone electric furnace with a stream of Ar gas flow. Typically, 200 mg of the as-prepared crude compound 2-TBQP was placed on a quartz boat and inserted into a 25 mm quartz tube. The tube was placed in the furnace and connected to a supply of Ar. The Ar flow was adjusted to 50 ml min^{-1}. The first zone contained the initial sample and was heated to 380 °C to promote volatilization. The second zone was the region of molecular transport and was heated to 340 °C. The third zone was heated to 250 °C to encourage crystal deposition. These heating and gas-flow conditions yielded needle-shaped crystals ~200 μm in the short dimensions and over 1 mm long on the quartz tube wall in about 8 h. Centimetre-long crystals can be obtained by extending the heating time to 24 h.

Thermal-initiated endogenous solid-state polymerization. A 10 mm quartz tube closed at one end and holding 2-TBQP crystals was paced in a tube furnace under an Ar flow of 100 ml min^{-1}. The closed end of the tube faces the inert of Ar flow to rule out disturbance by the gas flow during polymerization. The quartz tube was heated at 10 °C min^{-1} to 520 °C and maintained at 520 °C for 6 h to complete the polymerization. A tiny amount of the precursor was sublimated at the beginning of heating process, and deposited in the low-temperature area of the tube furnace. Finally, the tube furnace was cooled down to room temperature at 2 °C min^{-1}. The weight percentage of the residue was around 62%, close to the theoretical value (59.95%).

STM characterization. STM experiments were performed in a UHV chamber (base pressure of 10^{-10} mbar) with a UHV STM unit (SPECS high temperature-STM 150 Aarhus). The Au(111) and Au(110) surfaces (from Mateck) were cleaned by repeated Ar-ion sputtering at $P(\text{Ar}) = 1 \times 10^{-5}$ mbar, 1.5 keV, followed by annealing in the preparation chamber (base pressure 1×10^{-9} mbar) at 600 °C. 2-TBQP molecules were deposited onto the substrates with a Knudsen cell (from MBE-Komponenten) at 320 °C for 2–5 min. Polymerization was induced by annealing the samples at 250 °C. for 2 h. All the samples were characterized by STM at room temperature.

Molecular dynamics simulations. Molecular dynamics simulations were performed using the empirical force fields available in the ReaxFF package. The temperature was kept constant at 800 K using a temperature damping constant of 100 fs, the molecular dynamics time step was set to 0.25 fs, and the pressure was set to 0 MPa with a Berendsen pressure-damping constant of 500 fs.

DFT calculations. Details of the DFT calculations are given in the Supplementary Information.

Electrochemical characterization. To investigate the sodium-storage performance, a uniform slurry was prepared by mixing 2D-CAP (75 wt%), Super P carbon black (10 wt%) and sodium alginate binder (SA, 15 wt%) in water and stirring overnight. The slurry was coated on copper foil and dried at 80 °C in vacuum oven for 24 h. The coated copper foil was cut into discs 12 mm in diameter. The CR2016 coin cells were assembled in an Ar-filled glove box by using sodium metal as the reference electrode and counter electrode, with a glass microfiber filter (Whatman) as the separator. NaClO$_4$ (1.0 M) in anhydrous propylene carbonate was used as the electrolyte. The cells were galvanostatically discharged/charged at various current densities in the voltage range of 0.005–2.5 V (versus Na/Na$^+$) on a Bitrode battery tester system (Model SCN-12-4-5/18) with a data collection time interval of 0.3 s. The capacity was calculated based on the mass of active materials, which is 75% of the electrode.

Data availability. The authors declare that the data supporting the findings of this study are available within the article and its Supplementary Information files, or from the corresponding author on reasonable request. Crystallographic data for the structures reported in this paper have been deposited at the Cambridge Crystallographic Data Centre (CCDC) under the deposition numbers CCDC 1455701 (2-TBQP) and CCDC 1455702 (DDQP). Copies of the data can be obtained free of charge from www.ccdc.cam.ac.uk/data_request/cif.

References

1. Novoselov, K. S. *et al*. Electric field effect in atomically thin carbon films. *Science* **306,** 666–669 (2004).
2. Sakamoto, J., van Heijst, J., Lukin, O. & Schlüter, A. D. Two-dimensional polymers: just a dream of synthetic chemists? *Angew. Chem. Int. Ed.* **48,** 1030–11069 (2009).
3. Perepichka, D. F. & Rosei, F. Extending polymer conjugation into the second dimension. *Science* **323,** 216–217 (2009).
4. Colson, J. W. & Dichtel, W. R. Rationally synthesized two-dimensional polymers. *Nat. Chem.* **5,** 453–465 (2013).
5. Waller, P. J., Gándara, F. & Yaghi, O. M. Chemistry of covalent organic frameworks. *Acc. Chem. Res.* **48,** 3053–3063 (2015).
6. Baughman, R. H., Eckardt, H. & Kertez, M. Structure–property predictions for new planar forms of carbon: layered phases containing sp^2 and sp atoms. *J. Chem. Phys.* **87,** 6687–6699 (1987).
7. Chen, L., Hernandez, Y., Feng, X. & Müllen, K. From nanographene and graphene nanoribbons to graphene sheets: chemical synthesis. *Angew. Chem. Int. Ed.* **51,** 7640–7654 (2012).
8. Müllen, K. Evolution of graphene molecules: structural and functional complexity as driving forces behind nanoscience. *ACS Nano* **8,** 6531–6541 (2014).
9. Simpson, C. D. *et al*. Synthesis of a giant 222 carbon graphite sheet. *Chem. Eur. J.* **8,** 1424–1429 (2002).
10. Grill, L. *et al*. Nano-architectures by covalent assembly of molecular building blocks. *Nat. Nanotech.* **2,** 687–691 (2007).
11. Lafferentz, L. *et al*. Controlling on-surface polymerization by hierarchical and substrate-directed growth. *Nat. Chem.* **4,** 215–220 (2012).
12. Liu, X., Guan, C., Wang, D. & Wan, L. Graphene-like single-layered covalent organic frameworks: synthesis strategies and application prospects. *Adv. Mater.* **26,** 6912–6920 (2014).
13. Feng, X., Ding, X. & Jiang, D. Covalent organic frameworks. *Chem. Soc. Rev.* **41,** 6010–6022 (2012).
14. Wan, S. *et al*. Covalent organic frameworks with high charge carrier mobility. *Chem. Mater.* **23,** 4094–4097 (2011).
15. Xu, H., Gao, J. & Jiang, D. Stable, crystalline, porous, covalent organic frameworks as a platform for chiral organocatalysts. *Nat. Chem.* **7,** 905–912 (2015).
16. Guo, J. *et al*. Conjugated organic framework with three-dimensionally ordered stable structure and delocalized π clouds. *Nat. Commun.* **4,** 2736 (2013).
17. Groenewolt, M. & Antonietti, M. Synthesis of g-C$_3$N$_4$ nanoparticles in mesoporous silica host matrices. *Adv. Mater.* **17,** 1789–1792 (2005).
18. Bojdys, M. J., Jeromenok, J., Thomas, A. & Antonietti, M. Rational extension of the family of layered, covalent, triazine-based frameworks with regular porosity. *Adv. Mater.* **22,** 2202–2205 (2010).
19. Bhola, R. *et al*. A two-dimensional polymer from the anthracene dimer and triptycene motifs. *J. Am. Chem. Soc.* **135,** 14134–14141 (2013).
20. Kissel, P. *et al*. A nanoporous two-dimensional polymer by single-crystal-to-single-crystal photopolymerization. *Nat. Chem.* **6,** 774–778 (2014).
21. Kory, M. J. *et al*. Gram-scale synthesis of two-dimensional polymer crystals and their structure analysis by X-ray diffraction. *Nat. Chem.* **6,** 779–784 (2014).
22. Kissel, P. *et al*. A two-dimensional polymer prepared by organic synthesis. *Nat. Chem.* **4,** 287–291 (2012).
23. Gritsch, T., Coulman, D., Behm, R. J. & Ertl, G. A scanning tunneling microscopy investigation of the structure of the Pt(110) and Au(110) surfaces. *Surf. Sci.* **257,** 297–306 (1991).
24. Ben, T. *et al*. Targeted synthesis of a porous aromatic framework with high stability and exceptionally high surface area. *Angew. Chem. Int. Ed.* **48,** 9457–9460 (2009).
25. Yuan, D., Lu, W., Zhao, D. & Zhou, H. Highly stable porous polymer networks with exceptionally high gas-uptake capacities. *Adv. Mater.* **23,** 3723–3725 (2011).
26. Stille, J. K. & Mainen, E. L. Thermally stable ladder polyquinoxalines. *Macromolecules* **1,** 36–42 (1968).
27. Imai, K. *et al*. Synthesis and properties of thermally stable ladder polymers containing the 1,4-pyrazine ring obtained from polyheterocyclizations of tetramines and tetraketones in poly(phosphoric acid) and *m*-cresol. *Macromolecules* **6,** 158–162 (1973).
28. Côté, A. P. *et al*. Porous, crystalline, covalent organic frameworks. *Science* **310,** 1166–1170 (2005).
29. Meng, H., Perepichka, D. F. & Wudl, F. Facile solid-state synthesis of highly conducting poly(ethylenedioxythiophene). *Angew. Chem. Int. Ed.* **42,** 658–661 (2003).
30. Meng, H. *et al*. Solid-state synthesis of a conducting polythiophene via an unprecedented heterocyclic coupling reaction. *J. Am. Chem. Soc.* **125,** 15151–15162 (2003).
31. Newsome, D. A., Sengupta, D., Foroutan, H., Russo, M. F. & van Duin, A. C. T. Oxidation of silicon carbide by O$_2$ and H O$_2$: a ReaxFF reactive molecular dynamics study, part I. *J. Phys. Chem. C* **116,** 1611–1621 (2012).
32. Weismiller, M. R., van Duin, A. C. T., Lee, J. & Yetter, R. A. ReaxFF reactive force field development and applications for molecular dynamics simulations of ammonia borane dehydrogenation and combustion. *J. Phys. Chem. A* **114,** 5485–5492 (2010).
33. Islam, M. M., Bryantsev, V. S. & van Duin, A. C. T. ReaxFF reactive force field simulations on the influence of Teflon on electrolyte decomposition during Li/SWCNT anode discharge in lithium–sulfur batteries. *J. Electrochem. Soc.* **161,** 3009–3014 (2014).
34. Wu, S. M. *et al*. Molecular junctions based on aromatic coupling. *Nat. Nanotech.* **3,** 569–574 (2008).

35. Li, H., Powell, D. R., Firman, T. K. & West, R. Structures and photophysical properties of model compounds for arylethynylene disilylene polymers. *Macromolecules* **31,** 1093–1098 (1998).

36. Wang, C., Batsanov, A., Bryce, M. & Sage, I. Nanoscale aryleneethynylene molecular wires with reversible fluorenone electrochemistry for self-assembly onto metal surfaces. *Org. Lett.* **6,** 2181–2184 (2004).

37. Larcher, D. & Tarascon, J. M. Towards greener and more sustainable batteries for electrical energy storage. *Nat. Chem.* **7,** 19–29 (2015).

38. Yabuuchi, N., Kubota, K., Dahbi, M. & Komaba, S. Research development on sodium-ion batteries. *Chem. Rev.* **114,** 11636–11682 (2014).

39. Kundu, D., Talaie, E., Duffort, V. & Nazar, L. F. The emerging chemistry of sodium ion batteries for electrochemical energy storage. *Angew. Chem. Int. Ed.* **54,** 3431–3448 (2015).

40. Xu, F. *et al.* Electrochemically active, crystalline, mesoporous covalent organic frameworks on carbon nanotubes for synergistic lithium-ion battery energy storage. *Sci. Rep.* **5,** 8225 (2015).

41. Sakaushi, K. *et al.* Aromatic porous-honeycomb electrodes for a sodium–organic energy storage device. *Nat. Commun.* **4,** 1485 (2013).

42. Cao, Y. *et al.* Sodium ion insertion in hollow carbon nanowires for battery applications. *Nano Lett.* **12,** 3783–3787 (2012).

43. Ding, J. *et al.* Carbon nanosheet frameworks derived from peat moss as high performance sodium ion battery anodes. *ACS Nano* **7,** 11004–11015 (2013).

44. Song, Z. *et al.* Polymer–graphene nanocomposites as ultrafast charge-and-discharge cathodes for rechargeable lithium batteries. *Nano Lett.* **12,** 2205–2211 (2012).

45. Wang, D. *et al.* Layer by layer assembly of sandwiched graphene/SnO$_2$ nanorod/carbon nanostructures with ultrahigh lithium ion storage properties. *Energy Environ. Sci.* **6,** 2900–2906 (2013).

46. Wang, Z., Luan, D., Madhavi, S., Hu, Y. & Lou, X. W. Assembling carbon-coated α-Fe$_2$O$_3$ hollow nanohorns on the CNT backbone for superior lithium storage capability. *Energy Environ. Sci.* **5,** 5252–5256 (2012).

47. Simon, P. & Gogotsi, Y. Materials for electrochemical capacitors. *Nat. Mater.* **7,** 845–854 (2008).

Author contributions

K.P.L. supervised the project. W.L. and K.P.L. designed and performed the experiments. X.L. performed the theoretical calculations under the supervision of S.Y.Q. Y.B. performed the STM characterization. Y.P.L., I.A. and L.L. helped to exfoliate the sample and conduct the AFM imaging. G.H.N. helped with the crystal files analysis. C.T.N. helped to collect XPS spectra. Z.G.H. and D.Z. helped to perform Ar-sorption measurements. B.L. helped to analyse the experimental results. W.L., X.L., S.Y.Q. and K.P.L. wrote the manuscript with input from all the authors.

Additional information

Supplementary information is available in the online version of the paper. Reprints and permissions information is available online at www.nature.com/reprints. Correspondence and requests for materials should be addressed to S.Y.Q. (calculations) and K.P.L. (experiment).

Competing financial interests

The authors declare no competing financial interests.